NanoImpact 25 (2022) 100386

Contents lists available at ScienceDirect

NanoImpact

journal homepage: www.elsevier.com/locate/nanoimpact

Influence of natural organic matter on the transformation of metal and metal oxide nanoparticles and their ecotoxic potency *in vitro*

Alexander Khort [a,c,1,*], Marianne Brookman-Amissah [b,1], Jonas Hedberg [a,f], Tingru Chang [a], Nanxuan Mei [a], Annie Lundberg [a], Joachim Sturve [b], Eva Blomberg [a], Inger Odnevall [a,d,e,*]

[a] KTH Royal Institute of Technology, Department of Chemistry, Division of Surface and Corrosion Science, Drottning Kristinas vag 51, SE-100 44 Stockholm, Sweden
[b] University of Gothenburg, Department of Biological and Environmental Sciences, Gothenburg, Sweden
[c] National University of Science and Technology "MISiS", Research Center of Engineering Ceramic Nanomaterials, Moscow, Russia
[d] AIMES - Center for the Advancement of Integrated Medical and Engineering Sciences at Karolinska, Institutet and KTH Royal Institute of Technology, Stockholm, Sweden
[e] Karolinska Institutet, Department of Neuroscience, SE-171 77 Stockholm, Sweden
[f] Surface Science Western, The University of Western Ontario, London, Ontario, Canada

ARTICLE INFO

Keywords:
Metallic nanoparticles
Freshwater
Natural organic matter
Transformation
Reactive oxygen species
Cytotoxicity

ABSTRACT

Increased use and production of engineered nanoparticles (NPs) lead to an elevated risk of their diffuse dispersion into the aquatic environment and increased concern on unknown effects induced by their release into the aquatic ecosystem. An improved understanding of the environmental transformation processes of NPs of various surface characteristics is hence imperative for risk assessment and management. This study presents results on effects of natural organic matter (NOM) on the environmental transformation and dissolution of metal and metal oxide NPs of different surface and solubility properties in synthetic freshwater (FW) with and without NOM. Adsorption of NOM was evident on most of the studied NPs, except Sb and Sb_2O_3, which resulted in the formation of negatively charged colloids of higher stability and smaller size distribution compared with the same NPs in FW only. The dissolution rate of the NPs in the presence of NOM correlated with the strength of interactions between the carboxylate group of NOM and the particle surface, and resulted in either no (Mn, Sb, ZnO NPs), increased (Co, Sn NPs) and decreased (Ni, NiO, Sb_2O_3, Y_2O_3 NPs) levels of dissolution. One type of metal NP from each group (Mn, Ni, Sn) were investigated to assess whether observed differences in adsorption of NOM and dissolution would influence their ecotoxic potency. The results showed Mn, Ni, and Sn NPs to generate intracellular reactive oxygen species (ROS) in a time and dose-dependent manner. The extent of ROS generation in FW was similar for both Mn and Ni NPs but higher for Sn NPs. These findings are possibly related to interactions and infiltration of the NPs with the cells, which lead to redox imbalances which could induce oxidative stress and cell damage. At the same time, the presence of NOM generally reduced the intracellular ROS generation by 20–40% for the investigated NPs and also reduced cytotoxicity of Sn NPs, which can be attributed to the stronger interaction of carboxylate groups of NOM with the surface of the NPs.

1. Introduction

From increased use and production rates of engineered nanoparticles (NPs) follows an elevated risk of their diffuse dispersion into the aquatic environment (Vance et al., 2015; Gottschalk et al., 2013). This has increased the concern on unknown effects induced by their release into the aquatic ecosystem (Turan et al., 2019). Dispersed NPs transform in different ways upon environmental entry due to the adsorption of ligands, changes in surface charge, dissolution, and agglomeration (Hedberg et al., 2019; Lowry et al., 2012; Dale et al., 2015). These transformation processes have essentially been shown to govern the fate and the ecotoxic potency of NPs (Petosa et al., 2010). Interactions with natural organic matter (NOM) have previously been shown to influence the environmental fate of dispersed metallic NPs (Lowry et al., 2012; Lynch et al., 2014a; Wang et al., 2016) as NOM readily can adsorb to the NPs and thereby influence their transformation and dissolution

* Corresponding authors at: Drottning Kristinas vag 51, SE-100 44 Stockholm, Sweden.
E-mail addresses: khort@kth.se (A. Khort), ingero@kth.se (I. Odnevall).
[1] Both authors A. Khort and M. Brookman-Amissah have contributed equally towards the article and share the first author position.

https://doi.org/10.1016/j.impact.2022.100386
Received 20 October 2021; Received in revised form 25 January 2022; Accepted 26 January 2022
Available online 31 January 2022

characteristics, stability and mobility (Hotze et al., 2010; Khort et al., 2021; Xu et al., 2020; Svendsen et al., 2020; Pradhan et al., 2018; Hedberg et al., 2017a), as well as either mitigate or reduce their toxic potency (Svendsen et al., 2020; Arvidsson et al., 2020; Lowry, 2018; Garner and Keller, 2014). An improved understanding of these processes is hence imperative for risk assessment and management (Wang et al., 2016; Xu et al., 2020; Arvidsson et al., 2011; Garner et al., 2017).

In order to comply with the registration and safety assessment of nanomaterials required by the chemical regulation REACH (Registration, Evaluation, Authorization and Restriction of Chemicals), manufacturers, importers and downstream users of NPs are since 2020 obliged to prove their safe use over their entire life cycle (Clausen and Hansen, 2018; Nielsen et al., 2021). From this follows an urgent need for transformation/dissolution data as well as on oxidative stress and toxicity for NPs of different characteristics at aquatic relevant conditions.

Investigations have so far predominantly focused on NPs that are produced in the highest quantities, including, for example, SiO_2, Ag, ZnO, and TiO_2 NPs (Gottschalk et al., 2013; Furberg et al., 2019; Gondikas et al., 2018), whereas limited information related to NOM interactions exists for other metal and metal oxide NPs. Grouping and read-across require though larger sets of data for NPs of different physicochemical properties.

There is currently a gap in the available data for adequate assessments of NP toxicity in the aquatic environment, with very few studies focusing on *in vitro* models. The majority of available *in vitro* studies are limited and often focused on ultimate cell death resulting in the need for investigations into more sensitive sublethal endpoints. Oxidative stress is frequently reported as the main mechanism of NP-induced toxicity (Bundschuh et al., 2018). Studies on various organisms support that NPs are potent to cause toxicity by the formation of reactive oxygen species (ROS) due to *e.g.* cellular damage, but there are limited studies on *in vitro* models that confirm this in aquatic settings.

The aim of this study was to answer whether the adsorption of NOM (surface weathering) mitigates or promotes the environmental transformation/dissolution of a range of different metal (metal core with surface oxide) and metal oxide NPs in FW, and whether information on their environmental transformation potential and polarizing capacity could be used for grouping, read-across, modelling and risk assessment of relevance from a regulatory perspective (Hedberg et al., 2019; Garner and Keller, 2014). It also addresses the possibility that the adsorption of NOM to metallic NPs influences their ecotoxic potency on aquatic organisms (Bundschuh et al., 2018).

The study comprises both less and more extensively studied metallic NPs. The former NPs include Sb-based NPs (for example, used in sensors and semiconductors (Chin et al., 2010)), Sn-based NPs (*e.g.* in batteries (Zhang et al., 2008)), Co- and Ni-based NPs (*e.g.* magnetic applications (Khort et al., 2018; Johnston-Peck et al., 2009)), Mn NPs (*e.g.* water treatment), and Y_2O_3 NPs (*e.g.* utilized as alternatives to quantum dots (Traina and Schwartz, 2007)), whereas the latter NPs include ZnO and CeO_2, which are produced in larger volumes and for which environmental transformation data has been reported (Oriekhova and Stoll, 2016). Short-term (up to 6 h) environmental transformation and dissolution studies of metal and metal oxide NPs induced by the presence and adsorption of NOM (Suwannee river) were performed in terms of changes in size, zeta potential, adsorption of NOM and dissolution in synthetic freshwater (FW). The experimental design is to a large extent derived from the OECD protocol for short-term NP colloidal stability (Monikh et al., 2018; OECD, 2017) measurements in synthetic FW (OECD, 2002). All studies were performed at low enough NP concentrations (≈ 2 mg/L) to ensure no risk of saturation of released metal species. Too high concentrations can result in saturation and a reduced apparent NP dissolution compared with realistic conditions in which metal concentrations generally are undersaturated (Vencalek et al., 2016; Kent and Vikesland, 2016). Based on differences in transformation/dissolution patterns and NOM interactions of the different NPs, the effect of weathering on the ecotoxic potency was investigated for a selection of the NPs (Sn, Mn and Ni). These studies included particle concentrations from 0.2 up to 20 mg/L.

2. Materials and methods

2.1. Nanoparticles

Co, Cr_2O_3, Mn, Sn, and SnO_2 NPs were all purchased from American Elements (Los Angeles, USA) at a purity of 99.9%. Sb NPs were obtained from Campine (Beerse, Belgium). NPs of Sb_2O_3, Co_3O_4 NPs (purity of 99.5%), Ni (purity >99%) and NiO (purity >99.8%) were purchased from Sigma Aldrich (Sweden). ZnO NPs (JRCNM01101a) and CeO_2 NPs (JRCNM01101a) were obtained from the Joint Research Centre (EU commission, JRC Nanomaterials Repository, Italy). The Y_2O_3 NPs (purity 99.99%) were purchased from US nano (Houston, USA).

2.2. Chemicals and solutions

FW was prepared by mixing 0.0065 g/L $NaHCO_3$ (Sigma Aldrich, Sweden), 0.00058 g/L KCl (Sigma Aldrich, Sweden), 0.0294 g/L $CaCl_2{\cdot}2H_2O$ (Sigma Aldrich, Sweden) and 0.0123 g/L $MgSO_4{\cdot}7H_2O$ (Sigma Aldrich, Sweden). The pH was adjusted to 6.2 using 50% NaOH (Batch No. 08D280509, made in EC-EMB 45053, EC label: 215–185-5, Prolabo) or 5% aqueous solution of ultrapure HNO_3.

Suwannee river NOM was acquired from the International Humic Substances Society, USA, a heterogeneous mixture of different molecules, mainly fulvic and humic acids (Hay and Myneni, 2007). 10 mg/L NOM was added in FW, and the pH was adjusted to 6.2 by means of 5% HNO_3 and 50% NaOH.

Aqua Regia (25 vol% HCl and 65 vol% ultrapure HNO_3 with a volume ratio of 3:1) was used to digest some of the NPs in this study. Hydrogen peroxide (30 vol% H_2O_2 Merck, Germany) was used for the digestion of the CeO_2 and Y_2O_3 NPs.

Fetal bovine serum (FBS), trypsin, cell culture phenol red-free Leibovitz-15 medium (L-15) (Gibco, ThermoFisher Scientific, Sweden) were used in the cell culture process. L-15/ex saline buffer and 0.2% ethylenediaminetetraacetic acid (EDTA) (Sigma Aldrich, Sweden) in phosphate-buffered saline (PBS) solution were prepared according to standard protocols (Schirmer et al., 1997). AlamarBlue (Invitrogen, Sweden) and 5-carboxyfluorescein diacetate acetoxy methyl ester (CFDA-AM) (ThermoFisher Scientific, Sweden), Neutral Red solution (Sigma Aldrich, Sweden) and acidified ethanol solution (1% glacial acetic acid: 50% ethanol: 49% Milli-Q water solution) were used in fluorescence based assays to detect toxicity. 6-carboxy-2′7′-dichlorofluorescein diacetate (DCFH-DA) dissolved in DMSO (Sigma Aldrich, Sweden) were used to detect ROS formation. Tert-butyl hydroperoxide (t-BHP) in decane solution (Sigma Aldrich, Sweden) and copper sulphate (Sigma Aldrich, Sweden) served as positive controls.

2.3. Dissolution

The first step involved dispersion of the NPs (1 g/L) into solution by dispersing 6 mg NPs in 6 mL ultrapure water (18 MΩcm, MilliQ, Solna, Sweden) in acid-cleaned glass vials. The solutions were tip sonicated (Branson Sonifier 250, constant mode, output 2) for 5 min, representing a delivered acoustic energy of 2400 J (Pradhan et al., 2016). 100 μL stock solution was then transferred to 9.9 mL FW or FW containing NOM. 1.4 mL of this solution was thereafter transferred to 5.6 mL FW or FW + NOM, respectively. During these two steps, the stock solution was diluted 500 times. The solutions were exposed for 6 h in a Stuart S180 incubator with bilinear shaking at 25 °C (12° inclination, 22 cycles/min). After the exposure, 4 mL of the solution was ultra-centrifuged using a Beckman Optima L-90 K ultracentrifuge at 50,000 rpm for 1 h, a treatment shown to remove particles larger than ≈10 nm (Tsao et al., 2011). This treatment makes the exposure time in solution somewhat longer than the nominal time period for dissolution (6 h). 3 mL of the

supernatant of the centrifuged solutions was then transferred into acid-cleaned vessels and acidified to pH < 2 before analysis for their total metal concentrations in solution using atomic absorption spectroscopy (AAS) (described below).

Previous investigations have concluded that imperfect dispersion of metal NPs, *e.g.* due to agglomeration, dissolution/complexation and subsequent sedimentation, can lead to a lower administered dose compared with the nominal concentration transferred from stock solutions (Oriekhova and Stoll, 2016). 1.4 mL solution was therefore transferred from the original, sonicated stock solution into a vessel to determine the actual dose of the administered NPs. These dose samples were digested using 1.4 mL aqua regia.

The extent of dissolution connected to the sonication procedure was determined by transferring 1 mL of the original stock solution to 9 mL of ultrapure water. This solution was filtered using 20 nm Anotop filters (Whatman, USA). The filtered solution was acidified to pH < 2 and later analyzed by means of AAS. Each set of experiments to be analyzed for released metal concentrations in solution using AAS included triplicate samples to assess the dose of each exposed NP solution.

2.4. Metal quantification

Graphite furnace atomic absorption spectroscopy (GF-AAS) using a Perkin Elmer Analyst 800 instrument was used to analyze released concentrations of Co, Ni, Sb, Sn, Mn, Zn in solution. Standard solutions of known metal concentrations were prepared in 1% ultrapure HNO_3 together with a blank sample (1% ultrapure HNO_3). Calibration standards were used for quality control and run every 4th sample to ensure no memory effects. Calibration and analysis were repeated if the quality control sample deviated more than 10%. The dose samples were digested at a sample solution to aqua regia volume ratio of 1:1. The digestion procedure was validated by investigating known amounts of digested NPs (as described above) which proved complete dissolution of the NPs in the dose samples (> 94%). Limits of detection (LOD) were estimated from three times the standard deviation of the blank samples. The LODs were 1.2 μg/L for Sn and Cr, 2.5 μg/L for Ni, 2.8 μg/L for Sb, 3.1 μg/L for Zn and 3.6 μg/L for Co.

Released concentrations of Ce and Y were determined using ICP-MS (Perkin Elmer 350D, USA) in normal mode using 2% HNO_3 in ultrapure water as diluting medium. Indium (In) was used as an internal standard to correct for instrumental drift. The LODs were 0.01 μg/L for Ce and 0.003 μg/L for Y.

Control samples with metal ions of known concentrations added into FW and FW with NOM were prepared using the same protocol as for the NPs, including centrifugation, and analyzed by either AAS (Sn, Cr, Ni. Sb, Zn, Co) or ICP-MS (Ce, Y). The results showed a recovery of 80–100% for all metals. Recovery tests were also performed for the digested metal and metal oxide NPs related to the determination of administered doses (described above) with recoveries of 80–100%.

2.5. Zeta potential

The zeta potentials of the NPs were determined using laser Doppler microelectrophoresis, utilizing a Zetasizer Nano ZS instrument (Malvern Instruments, U.K.) operating at 25 °C. Duplicate measurements were performed in 10 mM NaCl (pH 5.6), FW (pH 6.2), and FW + 10 mg/L NOM (pH 6.2) with NPs exposed in solution for approximately 3 h. The Smoluchowski approximation was used to estimate the zeta potential from the electrophoretic mobility, motivated by the relatively large-sized agglomerates (several hundred nm).

2.6. Particle size and morphology

Nanoparticle tracking analysis (NTA) was employed using a NanoSight N300 (Malvern, Sweden) instrument to determine particle size distributions in solution. Five videos (each 60 s) were acquired for each individual sample, and three individual samples were prepared for each solution. As the method has its limitations - measured particles sizes depend on a specific method of NPs dispersion, solution composition, and particles characteristics. Thus NTA cannnot be used for general NPs size characterization.

Particle size and morphology of pristine NPs were investigated using a Hitachi HT7700 transmission electron microscope (TEM), operating at 100 kV. The TEM samples were prepared by dispersing the NPs in butyl alcohol at a concentration of 1 g/L using sonication (as described earlier), followed by deposition onto Formvar copper grids (Ted Pella, USA). The grids were left to dry overnight before analyzed.

2.7. Ligand adsorption

Attenuated total reflection Fourier transform infrared spectroscopy (ATR-FTIR) was utilized to study the adsorption of ligands in FW with and without the presence of NOM onto films of the different NPs. These studies were performed using a Bruker Tensor 37 FTIR spectrometer, a Platinum ATR-FTIR accessory, and a DTGS detector equipped with a polyethylene window. The ATR-FTIR accessory was equipped with a diamond crystal, and the angle of incidence for the IR beam was 45°. 512 scans were collected for each spectrum. The NPs (25 mg in 10 mL ethanol) were dispersed utilizing tip sonication for 5 min (Branson Sonifier 250, constant mode, output 2) as described above. 300 to 350 μL of the sonicated NPs solution was directly after dispersion drop cast onto the ATR crystal using a pipette. The NP film was left to dry for 2 h at ambient laboratory conditions. This procedure allowed ethanol evaporation and NP layer formation on the crystal. Background spectra were collected for the NP layer in ultrapure water (18.2 MΩcm resistivity, Millipore, Sweden). The solution (FW or FW with NOM) was then introduced onto the NP layer to collect the spectra. All experiments were performed in duplicate, and a spectrum was collected every 20th min up to 6 h. Data after 6 h are presented in this study. At the end of the experiments, ultrapure water was used to rinse the layer to assess if the adsorption was irreversible or not.

Using a built-in feature in the spectrometer, ATR correction was applied to the spectra to correct for the wavelength-dependent penetration depth of the evanescent wave (Mudunkotuwa et al., 2014). A refractive index of 2–2.1 was used in the correction as it showed the best correction of dispersion shaped peaks due to wavelength dependence of the penetration depth. The refractive index is lower than the bulk material due to the NP film porosity (Hug and Sulzberger, 1994).

2.8. Surface area

A 3Flex analyzer (Micromeritics, USA) was used to determine the BET (Brunauer Emmet Teller) specific surface area of the NPs (Brunauer et al., 1938). 0.5 g of each NP was degassed for 24 h under vacuum (0.05 mbar) at 300 °C before each measurement, except for the Sn NPs, which were degassed at 180 °C due to its low melting temperature. The specific surface area was calculated using the 3Flex software.

2.9. Cell culture and nanoparticle exposure

Rainbow trout (*O.mykiss*) gills Waterloo 1 (RTgill-W1) cells were cultured at 19 °C in 75 m^3 culture flasks containing L-15 medium supplemented with 5% FBS. Culture medium was replaced every 7–10 days, and cells were sub-cultured to form a confluent monolayer (Schirmer et al., 1997). Prior to exposure, 96-well plates were seeded with RTgill-W1 cells at a density of 50,000 cells/well and incubated with L-15 medium containing 5% FBS at 19 °C for 24 h in a Memmert incubator.

Mn, Ni and Sn NPs were dispersed in FW with and without NOM as previously described and further diluted in L-15 medium after 6 h incubation to obtain the desired concentration range. Pre-incubated cells were exposed for 24 h to 100 μL of three particle concentrations (0.2, 2 and 20 mg/L) of each NP (with and without NOM) in 6 replicates. Three

technical and three biological replicates were included to account for variability in the results.

2.10. Cytotoxicity in piscine cell line

24 h after NP exposure, AlamarBlue, CFDA-AM and Neutral Red assays were performed on the same set of cell replicates, following previously reported modifications to the protocol (Dayeh et al., 2013). The exposure medium was removed, and the cells were rinsed twice with 150 μL L-15/ex solution and observed under an inverted microscope to account for losses. 100 μL probe solution (1.25% (v/v) Alamar Blue and 4 μM CFDA-AM in L-15/ex solution) was added to each well, and the 96-well plates were incubated at 19 °C for 30 min at dark conditions. After incubation, the fluorescence intensity was measured using a Spectramax Gemini M microplate reader at excitation/emission wavelengths of 532/590, 485/535 nm for AlamarBlue and CFDA-AM, respectively. (Kamiloglu et al., 2020)

After the measurements, the same set of cells was washed twice with 150 μL L-15/ex to remove the previous probe solution. 100 μL of 0.03 mg/mL Neutral red (NR) in L-15/ex solution was added to each well, and the plates were incubated at 19 °C for 1 h at dark conditions. After 1 h, retained NR inside the cells was extracted by adding 150 μL acidified ethanol solution to each well. Fluorescence intensity was measured using a Spectramax Gemini M microplate reader at excitation/emission wavelengths of 532/680 nm for the Neutral red signal. All fluorescence values were corrected with the cell-free control, normalized against the medium control to deduce a percentage of cell viability.

2.11. Measurement of oxidative stress (ROS generation in piscine cell line)

To detect the reactive oxygen species generation after cellular exposure to the Mn, Ni and Sn NPs with and without NOM, 100 μL of 20 μM DCFDA in serum-free L-15 medium (loading solution) was preloaded in seeded 96-well plates prior to NP exposure. Cells were incubated at dark conditions for 30 to 45 min to ensure DCFDA diffusion into the cells. The loading solution was removed and replaced with a 100 μL exposure solution. Two experimental scenarios were investigated including measurements of the kinetics of the fluorescence intensity up to 6 h after immediate NP exposure and the kinetics for a period of 18 h after the 6 h incubation of the NPs (24 h total exposure). Single endpoint reading was made at selected time points using a Spectramax Gemini M microplate reader at excitation/emission wavelengths of 485/535 nm. Fluorescence values were corrected with the cell-free control and normalized against the medium only (vehicle) used as control.

2.12. Statistical analysis

Student's *t*-test analysis was performed using the Origin software in an ANOVA mode to compare the difference in metal release for the different solutions. Data from the cell-based assays were analyzed by the Student's t-test and one-way ANOVA using GraphPad Prism 9 software to assess differences between the metals and the influence of NOM.

3. Results and discussion

3.1. NPs characteristics

The size and shape of the NPs at dry conditions were investigated by means of TEM, Fig. 1. From the images, it is evident that the NPs considerably differ by their morphology: irregularity of shapes, NPs size distribution, and degree of agglomeration. For instance, the NiO and CeO_2 NPs displayed relatively similar shapes and size distributions, whereas the larger-sized NPs of Sb_2O_3 showed significant heterogeneity in terms of both size and shape. Furthermore, Mn, SnO_2, and Y_2O_3 NPs are highly agglomerated, as the degree of agglomeration of Ni, NiO, and

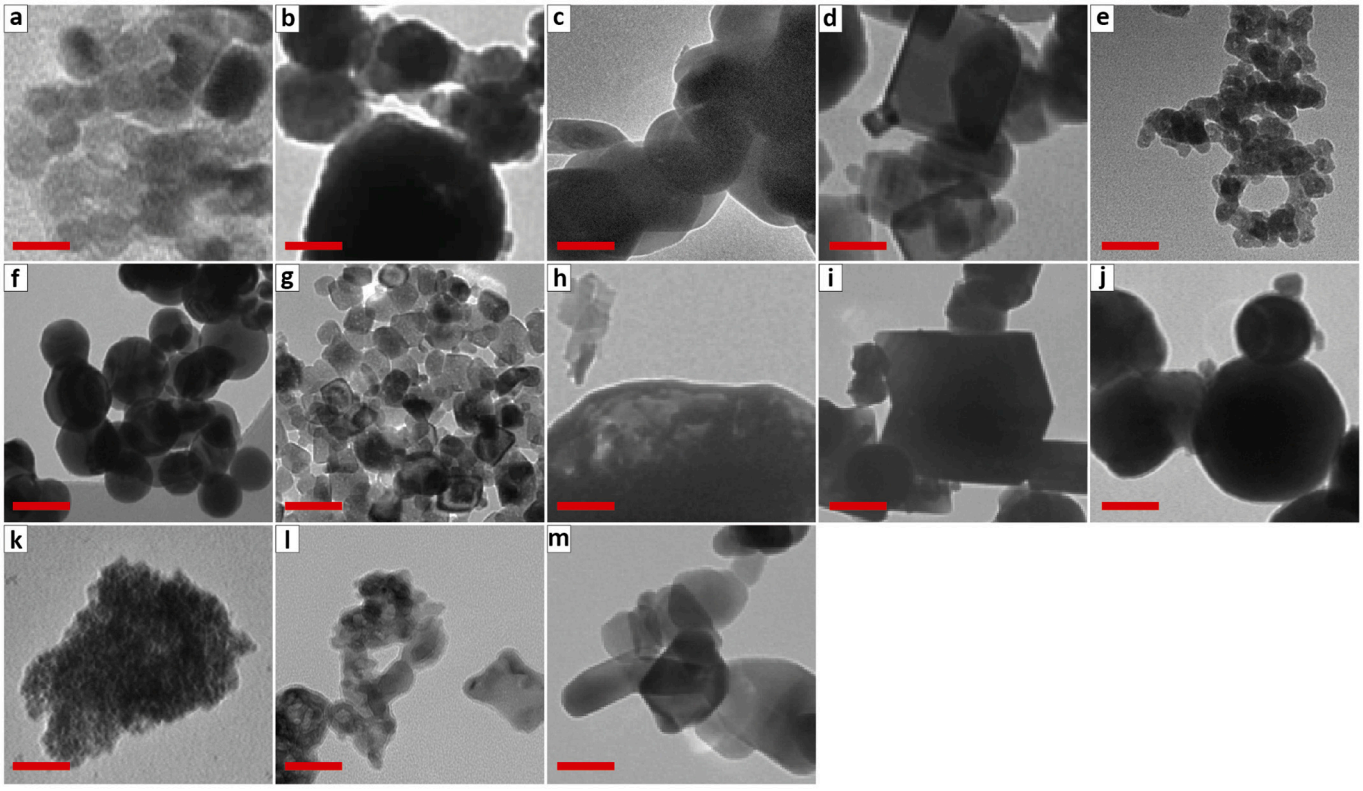

Fig. 1. Typical TEM images of (a) CeO_2, (b) Co, (c) Co_3O_4, (d) Cr_2O_3, (e) Mn, (f) Ni, (g) NiO, (h) Sb, (i) Sb_2O_3, (j) Sn, (k), SnO_2, (l) Y_2O_3, (m) ZnO NPs. Scale bar equals 50 nm.

ZnO NPs is noticeably lower. Such variation of NPs characteristics could influence their hydrodynamical stability in solution, interactions with dissolved functional groups, dissolution, and, as a result, toxic potency and, thus, requires careful consideration.

Surface compositional measurements of the outermost oxide (top 5–10 nm) were performed by employing XPS, surface area utilizing BET and the zeta potential in solution, both in NaCl (pH 5.6) and in fresh water (pH 6). Measurements in NaCl were performed to give insight into the intrinsic zeta potential properties of the NPs and were therefore conducted at as simple chemical conditions as possible (low ionic strength, non-buffered or pH adjusted. The slightly lower pH of NaCl (pH 5.6) compared to FW (pH 6.2) will not influence the dissolution of the NPs to any large extent. The results are summarized in Table 1 for all the investigated particles.

The metal NPs with surface oxides (core/shell NPs) had, in many cases, a somewhat different composition compared with their corresponding metal oxide NPs, *e.g.* both CoO and Co_3O_4 were identified on the surface of the Co NPs (Hedberg et al., 2017a). Due to peak overlap and a broad peak, SnO and/or SnO_2 could be constituents of the surface oxide of the Sn NPs. The majority of the NPs was negatively charged in NaCl (10 mM) at pH 5.6. The NiO and the Cr_2O_3 NPs were weakly charged, whereas both the Sn and the Y_2O_3 NPs were positively charged.

In the following, results on NP stability in solution and dissolution are presented in freshwater with and without NOM as it is important to address whether aquatic organisms such as fish will be exposed to primary NPs and/or aggregates of NPs, and/or dissolved metals forming colloids and complexes, *etc* and whether interactions with NOM forming an "ecocorona" would influence the ecotoxic potency of the metallic NPs.

3.2. Colloidal and surface transformations in the presence of NOM

ATR-FTIR was employed for *in-situ* studies (up to 6 h) of the possible adsorption of NOM and FW constituents onto the different NP-films. Spectra are presented in Fig. 2 for each NP for time periods when most of the NPs (except Mn and Y_2O_3) showed no significant increase in the peak area of the asymmetric COO^- vibrational band related to NOM (typically taking place within 2–5 h), Fig. S1. This indicates that saturated quasi-steady states of the dynamic equilibrium of the NOM absorption-desorption process were reached. The spectral region between 800 and 1800 cm^{-1} is the region where the strongest vibrational bands from adsorbed species of NOM was observed. These peaks originate only from adsorbed species as the spectrum of the solution phase (FW + NOM without any NP film) did not reveal any detectable

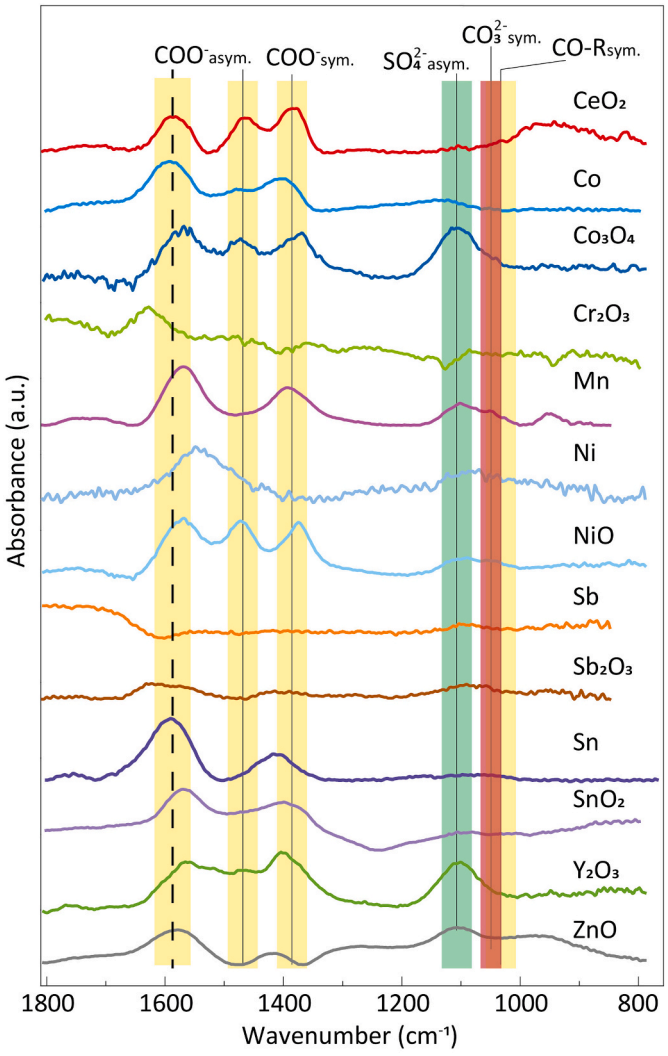

Fig. 2. *In situ* ATR-FTIR spectra of NP films in FW and NOM (10 mg/L Suwannee river NOM), pH 6.2. The dashed line at 1587 cm^{-1}, which represents the position of asymmetric COO^- vibrational band in solution (Hay and Myneni, 2007), id added for comparison with the position of the same band for adsorbed NOM in the spectra.

Table 1
Approximate particle size range and median size (TEM), surface oxide composition (XPS, ATR/FTIR), BET specific surface area, and zeta potentials in NaCl (10 mM, pH 5.6) and in FW (pH 6.2) of the investigated metallic NPs.

NPs	Particle size range/ TEM (nm)	Median particle size/ TEM (nm)	Surface oxide composition XPS, FTIR	Specific surface area/ BET (m^2/g)	Zeta potential in NaCl (mV)	Zeta potential in FW (mV)
CeO_2	10–25	15	CeO_2[a]	66.8	−14 ± 1	−5 ± 2
Co	15–200	44	CoO/Co_3O_4 (Hedberg et al., 2017a)	10.7	−17 ± 1	−13 ± 4
Co_3O_4	40–200	54	Co_3O_4 (Cappellini et al., 2018)	1.7	−24 ± 2	−13 ± 2
Cr_2O_3	10–100	23	Cr_2O_3[a]	5.8	−6 ± 4	−13 ± 1.4
Mn	10–50	15	MnO/MnO_2/Mn_2O_3/Mn_3O_4 (Hedberg et al., 2016)	26	−23 ± 3	−0.3 ± 1.2
Ni	20–200	42	NiO/$Ni(OH)_2$ (Latvala et al., 2016)	6.4	−20 ± 2	−13 ± 3
NiO	10–50	19	NiO/$Ni(OH)_2$ (Latvala et al., 2016)	102	−2 ± 4	−9 ± 3
Sb	90–1200	109	Sb_2O_3 (McCarrick et al., 2020)	0.7	24 ± 0.4	−6 ± 2
Sb_2O_3	20–250	38, 157[c]	Sb_2O_3 (McCarrick et al., 2020)	2.5	−23 ± 2	−7 ± 1
Sn	10–150	25	SnO/SnO_2[b], (McCarrick et al., 2020)	4.8	−35 ± 7	−3.3 ± 0.5
SnO_2	2–5, 50–200	4	SnO_2[a], (McCarrick et al., 2020)	116.9	−17 ± 5	−2.6 ± 0.2
Y_2O_3	10–80	15, 44[c]	Y_2O_3[a]	40.3	16 ± 1	19 ± 1
ZnO	15–150	34, 87[c]	ZnO[a]	12.7	−18 ± 1	5 ± 7

[a] Surface oxide composition equals the bulk composition.
[b] Not possible to unambiguously distinguish SnO from SnO_2 by employing XPS due to peak overlap.
[c] Median sizes in two main direction for the NPs with prolonged grain shape.

vibrational bands. The weak band at *ca.* 1050 cm^{-1} (symmetric stretch) and the stronger bands at *ca.* 1300–1500 cm^{-1} (asymmetric stretch) (Lefèvre, 2004), were assigned to carbonate and the band at 1100 cm^{-1} to sulfate (both originating from FW) (Lefèvre, 2004). Bands related to NOM, including C-O(−R,-H) containing compounds were observed at 1050–1150 cm^{-1}, symmetric COO^- at *ca.* 1350–1450 cm^{-1}, and asymmetric COO^- at *ca.* 1550–1600 cm^{-1} (Hay and Myneni, 2007; Mudunkotuwa and Grassian, 2015). Some overlap between the vibrational bands from the NOM and FW constituents is inevitable, however the asymmetric COO^- peak originating from NOM did not show any overlap. Since fulvic and humic acids are rich in carboxylates, this confirms the adsorption of NOM (Ritchie and Perdue, 2003). Rinsing the NP films with ultrapure water after 6 h left the spectra virtually unchanged, which indicates a relatively strong adsorption of NOM and FW-constituents to the NPs.

In contrast to the other NPs, only minor adsorption of NOM could be discerned for the Sb and Sb_2O_3 NPs.

Observations of adsorbed NOM on most of the NPs are in line with the particle size distribution results by means of NTA after 6 h exposure in FW with and without NOM, Fig. 3a and S2, and zeta potential measurements in the same solutions and in NaCl (10 mM, pH 5.6) after 2 h of exposure, Fig. 3b. The zeta potential investigations were conducted for FW + NOM solutions without any NPs and for suspensions with higher NP concentrations (10 mg/L) than the NTA investigations on particle size distribution (≈ 2 mg/L) in order to ensure reliable results with the technique.

The median particle sizes were smaller for all NPs, and the zeta potentials more negative in FW with NOM compared with FW only. This was expected, taking into account a highly negative zeta potential of FW with NOM (−20.0 mV). The results confirm the adsorption findings with NOM using ATR-FTIR and illustrate its possibility to stabilize the NPs in solution to different extents. The more negative zeta potentials observed for all NPs in the presence of NOM are primarily connected to negatively charged carboxylates (Ritchie and Perdue, 2003). A more negative zeta potential, also observed for the Sb NPs upon addition of NOM, imply possible adsorption of NOM even though it was not detectable using the ATR-FTIR set-up. Non-detectable adsorption of humic acid and non-colloidal stability have previously been observed for WC NPs (Hedberg et al., 2017b). One coherent characteristic between the Sb NPs and the WC NPs is their low isoelectric points (IEP) 1–3 (Kosmulski, 2009). This can result in a highly negatively charged NP surface at pH 6.2, giving rise to relatively strong repulsive electrostatic forces between the NPs and the negatively charged carboxylate groups of NOM ($pK_a \approx 4$) (Ritchie and Perdue, 2003). In the case of the other NPs (predominantly negatively charged, see Table 1 and Fig. 3b), adsorbed NOM can overcome the electrostatic repulsive forces due to other attractive interactions (*e.g.* hydrogen bonds, van der Waals forces) and gain in entropy which increase the Gibbs free energy of adsorption. The gain in entropy originate from the replacement of a higher number of small ions and water molecules with one larger sized NOM molecule.

The particle size distribution findings support the general observation that adsorption of NOM can provide some colloidal stability. This was most evident for the smaller sized NPs of the Cr_2O_3 (Fig. S2d), Sb_2O_3 (Fig. S2i), and ZnO NPs (Fig. S2m) in the presence of NOM, whereas the effect was less evident for the Sb NPs (Fig. S2h), Mn NPs (Fig. S2f) and SnO_2 NPs (Fig. S2l).

A schematic image summarizing observed trends in adsorption of NOM onto the NPs, as well as changes in zeta potential and particle size distribution is presented in Fig. 4. The surface charges depicted for the NPs before their interactions with FW and FW with NOM reflect their corresponding zeta potentials determined in 10 mM NaCl (pH 5.6), Table 1 and Fig. 3b.

The ATR-FTIR findings show that exposures of the NPs in FW with NOM result in the adsorption of carbonate, sulfate and NOM, Fig. 2, of which NOM had a considerable capacity to improve the colloidal stability, Fig. 3. Adsorption of such species is commonly referred to as the formation of an adsorbed layer, an eco-corona (Lynch et al., 2014b), though it cannot be ambiguously determined if a complete layer is formed or not. Judged from differences in relative strengths of the different bands observed in Fig. 2, the different NPs show some compositional differences. For example, bands related to sulfate and C—O groups (band at ≈1100 cm^{-1}) were more abundant for the ZnO, Y_2O_3, and Co_3O_4 NPs compared to the other NPs. However, these differences did not influence the general trend on colloidal stability, Fig. 3. An improved colloidal stability upon adsorption of NOM to metal and metal oxide NPs generally agrees with findings of previous studies on, *e.g.* CeO_2 (Oriekhova and Stoll, 2016), Mn NPs, and Cu NPs, and rely on both electrostatic and steric repulsion forces (Lowry et al., 2012). Some exceptions have been observed, for example, at high NOM concentrations (*e.g.* 40 mg/L) and hypothesized to result in cross-linking between the NPs (Schneckenburger et al., 2012). An improved colloidal stability can still result in both agglomeration, Fig. 3, and sedimentation, which are especially relevant for metal NPs that have relatively large attractive van der Waals forces (Pradhan et al., 2016).

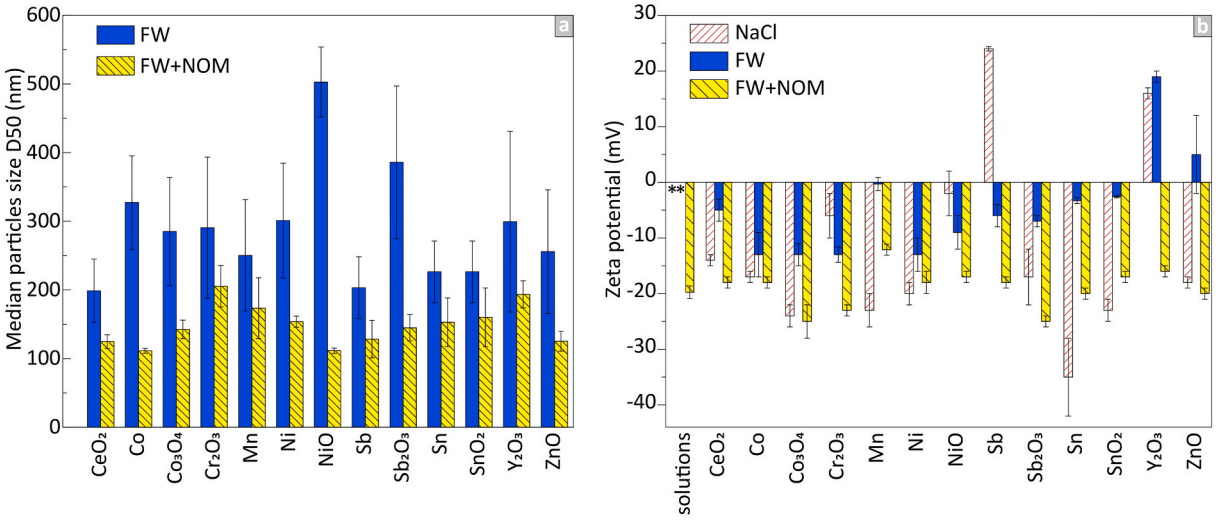

Fig. 3. a) Median particle sizes determined by means of NTA (NP concentrations: 2 mg/L) in FW with and without NOM (pH 6.2) after 6 h of exposure and b) Zeta potentials in 10 mM NaCl, and in FW with and without NOM after 2 h of exposure (NP concentrations: 10 mg/L). The error bars represent one standard deviation based on two independent experiments. * N/A.

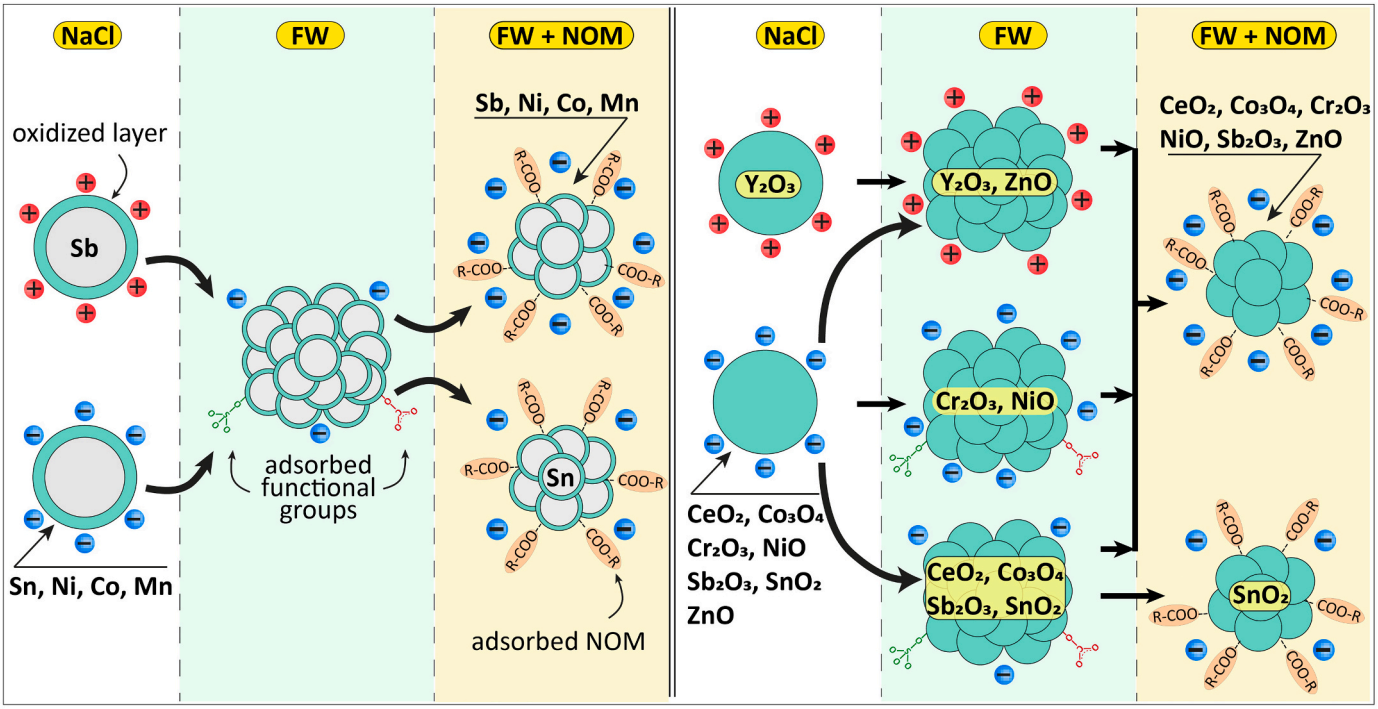

Fig. 4. Schematic illustration of trends in NP transformation and colloidal stability in FW with and without NOM. The adsorption of FW constituents and/or NOM on all NPs (low/no absorption on the Sb and Sb_2O_3 NPs) results in negatively charged colloids.

Relatively broad vibrational bands observed in the ATR-FTIR spectra (FWHM ≈ 70–80 cm^{-1}) are in line with previous findings and reflect the heterogeneous nature of NOM, with carboxylate groups in the vicinity of groups of different polarity (Hay and Myneni, 2007; Yoon et al., 2005). The position of the asymmetric COO^- band for the bulk solution FW + NOM is marked as a dashed line in Fig. 2 in order to compare with the same band observed for the NP layers related to adsorbed species. The asymmetric COO^- band position can shift upon interactions with metal ions both due to sharing of electrons between the metal ion and the carboxylate group, and due to peak splitting related to different kinds of coordination between the oxidized metal surface and the carboxylate groups of NOM. (OECD, 2017) The significance of the peak shift in relation to NP dissolution induced by interactions with NOM is discussed in the next section.

3.3. *Influence of NOM on dissolution*

The extent of dissolution from the metal and metal oxide NPs after 6 h in FW and FW + NOM is presented as the released metal fraction in relation to the total metal content of the NPs, Fig. 5a, and when normalized to both total metal content and surface area (BET, Table 1).

The dissolution results show markedly different behavior for the investigated NPs. Co NPs, Mn NPs, Sb NPs, ZnO NPs, and Y_2O_3 NPs dissolved relatively fast with > 20% dissolution of the total metal content after 6 h for the Sb and Y_2O_3 NPs and even higher (> 35–60%) for the Co, Mn and ZnO NPs, respectively. The high reactivity of the ZnO

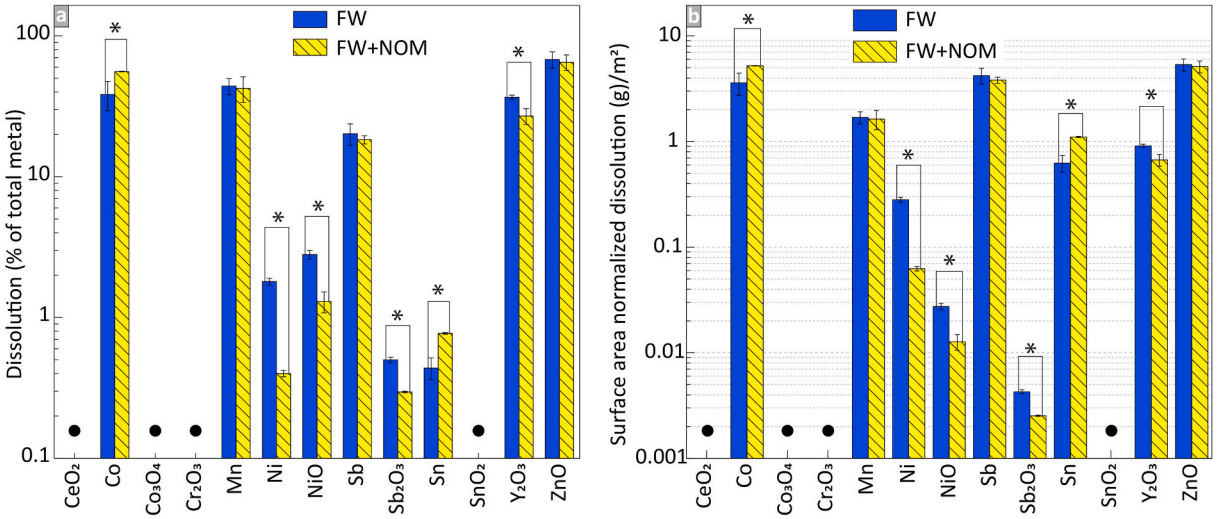

Fig. 5. (a) Dissolution (% of total metal content of the NPs) and (b) total metal content and surface area normalized dissolution after 6 h exposure in either FW or FW with NOM (Suwannee River NOM, 10 mg/L) at pH 6.2. The solid black circles indicate non-detectable metal concentrations in solution. The error bars represent one standard deviation derived from three independent experiments. The asterisks indicate statistically significant differences ($p < 0.05$, Student's *t*-test).

and Y_2O_3 NPs has previously been observed in media containing molecules relevant for NOM (Hedberg et al., 2019; Zhang et al., 2016). No detectable dissolution was observed for Co_3O_4, SnO_2, CeO_2, and Cr_2O_3 NPs (see Materials and Methods for LODs).

The extent of dissolution is affected by the surface area of the agglomerates formed in solution (Fig. 5b) (Dale et al., 2017), and a higher surface area generally results in more dissolution (Borm et al., 2006). This was the case for the Co NPs (6 times larger BET surface area) compared with the Co_3O_4 NPs. However, this was not the case for neither the NiO *vs* Ni NPs, the SnO_2 *vs* Sn NPs, nor the Sb_2O_3 *vs* Sb NPs, Fig. 5b, all showing larger BET surface areas for the oxides (16, 4, 25 times, respectively) compared with the core-shell oxidized metal NPs, Table 1. This implies the importance of other factors such as surface composition and different mechanisms that govern the dissolution behavior (Hedberg et al., 2019).

The results furthermore show the effect of NOM on the dissolution behavior to be largely material specific. No statistically significant effects of NOM were observed for the Mn, Sb or ZnO NPs, whereas the dissolution may be slightly enhanced in the case of the Co and Sn NPs, significantly reduced for the Ni, NiO and Sb_2O_3 NPs and slightly reduced ($p < 0.05$) for the Y_2O_3 NPs, Fig. 5a. Adsorption of NOM has been shown to influence the dissolution process *via* several mechanisms (Hedberg et al., 2019), possibly by interacting through different surface sites (Yoon et al., 2005; Stumm, 1995). Adsorption of fulvic acid on Al_2O_3 NPs has, for example, been reported to suppress dissolution by forming outer-sphere complexes (weak binding and no electron sharing) (Johnson et al., 2005). Inner-sphere complexes (strong interaction, electron sharing) with ligands, *e.g.* NOM constituents, have, on the other hand, been shown to correlate with enhanced dissolution (Gulley-Stahl et al., 2010). Adsorption of NOM can also influence corrosion reactions taking place on metallic surfaces (metal NPs with surface oxides) by weakening the surface oxide or blocking the surface from reactions (Hedberg et al., 2019), effects possibly observed for the Co and Sn NPs but not the case for either the Ni, Mn or Sb NPs, Fig. 5.

The asymmetric COO^- vibration of adsorbed NOM is the most sensitive vibration towards changes in its chemical environment (Hay and Myneni, 2007). Positive band shifts can hence be regarded as indicative of the formation of inner-sphere complexes (Johnson et al., 2005). In an attempt to deduce a pattern if the type of NOM binding to the surface could explain the dissolution pattern, the shift of the asymmetric COO^- band in relation to its frequency at bulk solution conditions, Fig. 2, was plotted *vs* the extent of dissolution in FW + NOM compared to FW only, Fig. 6a.

The results show a positive correlation between an enhanced dissolution induced by NOM and the shift in the asymmetric COO^- band from adsorbed NOM. Positive shifts were observed for the Co and Sn NPs for which the presence of NOM enhanced the extent of dissolution, whereas negative shifts were observed for the Ni, NiO and Y_2O_3 NPs, which revealed reduced dissolution, and for Mn and ZnO NPs for which no effects were observed in the presence of NOM. Data for the Sb and Sb_2O_3 NPs are not included in the Fig. 6a as no, or weak, adsorption of NOM was observed by means of ATR-FTIR, Fig. 2. Neither the CeO_2, Co_3O_4, Cr_2O_3, nor SnO_2 NPs are included due to non-detectable amounts of dissolved metals, Fig. 5. As previously mentioned, the shift in the asymmetric COO^- band compared to the bulk solution position correlates to some extent with the strength of the interaction, with large positive shifts indicative of increased dissolution. The trend in Fig. 6a, which includes both metal and metal oxide NPs, thus implies chemical dissolution (*e.g.* ligand exchange) (Hedberg et al., 2019) to be an important dissolution mechanism for these types of NPs. At the same time, there is a relation between the difference between the symmetric and asymmetric carbonate vibrations for an adsorbed carbonate complex and the polarizing power of the metal ion that it coordinates to (Lefèvre, 2004), and there is likely a similar pattern for carboxylate groups (Hay and Myneni, 2007; Yoon et al., 2005). The strength of the interaction with the surface as well as the properties of the metal ions thus influence the interaction with NOM. Effects of NOM on the dissolution pattern in relation to the polarizing power of the respective metal ions are presented in Fig. 6b. The trend is to some extent analogous to the results of Fig. 6a and shows a correlation between a higher polarizing power and enhanced dissolution. These results show the importance of understanding how metal ions interact with NOM, *e.g. via* binding with carboxylate groups, to better understand the extent of dissolution and its processes at environmentally relevant conditions. Sb and Sb_2O_3 NPs were, as previously discussed, to some extent exceptions in the interaction with NOM due to the weak (Sb_2O_3 NPs) and no detectable adsorption (Sb NPs) of NOM (based on ATR-FTIR results). Nevertheless, their dissolution patterns were in line with findings of Fig. 6b, which indicate that the use of polarizing power of metal ions can be a way forward to predict the effects of NOM on the dissolution pattern for metallic NPs. However, it should be noted that the approach of using the polarizing power of metal ions does not capture possible differences

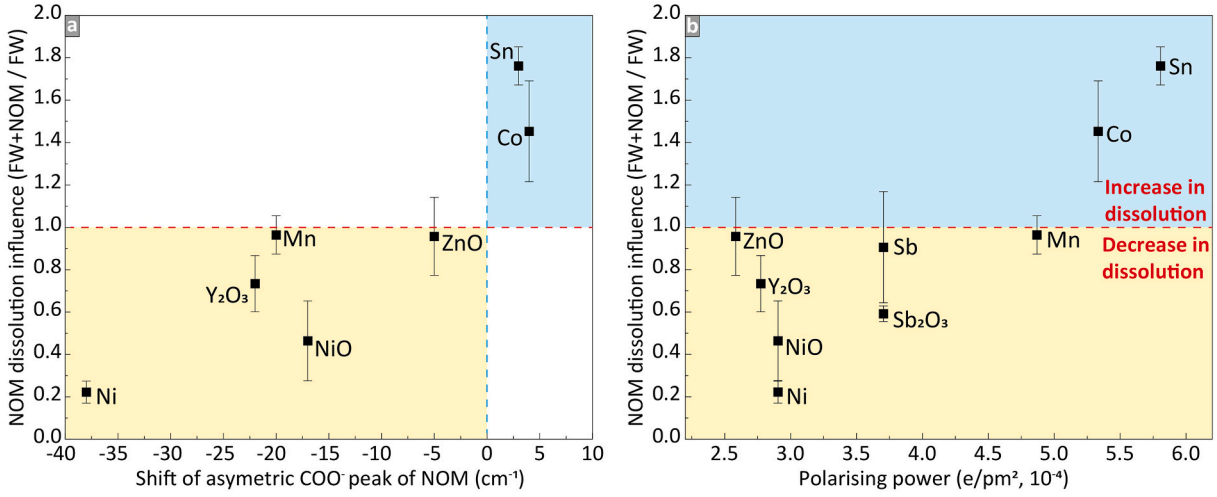

Fig. 6. (a): Dissolution of the different metal and metal oxide NPs in FW compared with their respective dissolution in FW + NOM (data from Fig. 5) after 6 h plotted against the shift of the asymmetric COO^- band in relation to its position in bulk solution (FW + NOM without NPs) (Fig. 2). (b): The effect of NOM on dissolution (same data as in (a)) *versus* the polarizing power of the corresponding metal ions (Ni^{2+}, Zn^{2+}, Mn^{2+}, Sb^{3+}, Sn^{2+}, and Co^{2+}). The polarizing power is here defined as z/r (Gottschalk et al., 2013), where z is the charge of the metal ion in (e) and r is the ionic radius in (pm). The ionic radius values were taken from the literature (Shannon, 1976).

between different oxides of the same metals (*e.g.* CoO, Co_3O_4, Fe_2O_3, Fe_3O_4). The results of Fig. 6 are only relevant for assessing trends in how the presence of NOM will influence the extent of dissolution and its mechanisms and cannot be used to assess the absolute dissolution behavior as there is no correlation between the dissolution, Fig. 5, and the shift in frequency of the carboxylate band, Fig. 2. The presented results of Fig. 6 can nonetheless be used to understand the effects of NOM on the short-term dissolution of various metal and metal oxide NPs, for example, to extrapolate results generated in FW to conditions of FW with NOM. A similar approach has been suggested for NP ecotoxicity assessments (Arvidsson et al., 2020).

In order to assess whether the adsorption of NOM and its effects on the dissolution pattern of the metallic NPs would influence their environmental fate in terms of ecotoxic potency, ecotoxicological measurements were conducted on selected NPs, which showed no effect (Mn NPs), increased dissolution (Sn NPs) and decreased dissolution (Ni NPs) in the presence of NOM.

3.4. Ecotoxicological assessment

In vitro fish cell systems are important bioanalytical tools in evaluating NP-induced ecotoxicological effects in the aquatic environment. The Sn, Mn and Ni NPs were selected and investigated as they showed significant differences in extent of dissolution, NOM peak shift and polarizing power (Fig. 6). The aim was to specifically assess if weathering (transformation/dissolution) and adsorption of NOM to the NPs would influence their toxic potency towards the piscine cell line RTGill-W1, with cytotoxicity and potential to generate ROS as endpoints (Dayeh et al., 2013).

All NPs generated intracellular ROS in a time- and dose dependent manner. Intracellular ROS generation was significantly reduced after 6 h in the presence of adsorbed NOM, Fig. 7. However, no significant differences were observed for the shorter time periods for conditions with and without NOM.

A statistically significant increase in ROS with respect to the control (medium only) was observed after 6 h for all NPs and NP concentrations ($p < 0.05$), and even higher ($p < 0.01$) between the NPs exposed with NOM. The Mn and Ni NPs, Fig. 7a, b showed a relatively similar extent of ROS generation in FW without NOM (up to 100 relative fluorescence units, RFU), whereas higher values (up to 150 RFU) were determined for the Sn NPs, Fig. 7c. The presence of NOM reduced the intracellular ROS generation by 20–40% for all NPs. A gradual reduction with time in intracellular ROS was observed after 6 to 8 h for the 24 h treatment, see Fig. S3 (Supporting information), which may be related to the

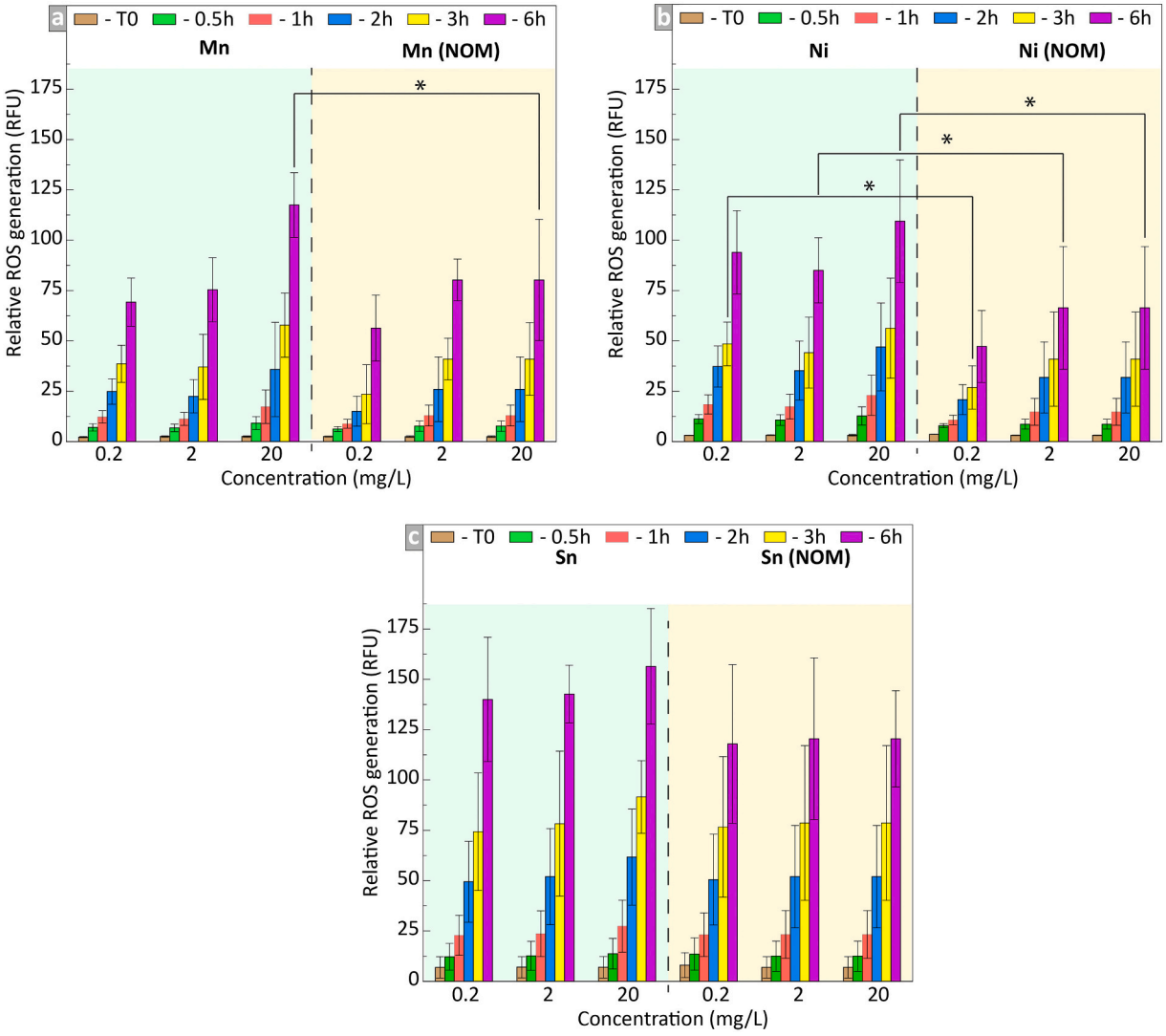

Fig. 7. Relative ROS generation over 6 h for particle concentrations of 0.2, 2 and 20 mg/L in FW with and without NOM (a): Mn-Mn(NOM), (b): Ni-Ni(NOM) and (c): Sn-Sn(NOM). The results are presented as mean and standard deviation of the means (SEM) of at least three independent experiments. Statistical significance between the groups are indicated with one ($p < 0.05$) or two ($p < 0.01$) asterisks (Student's *t*-test).

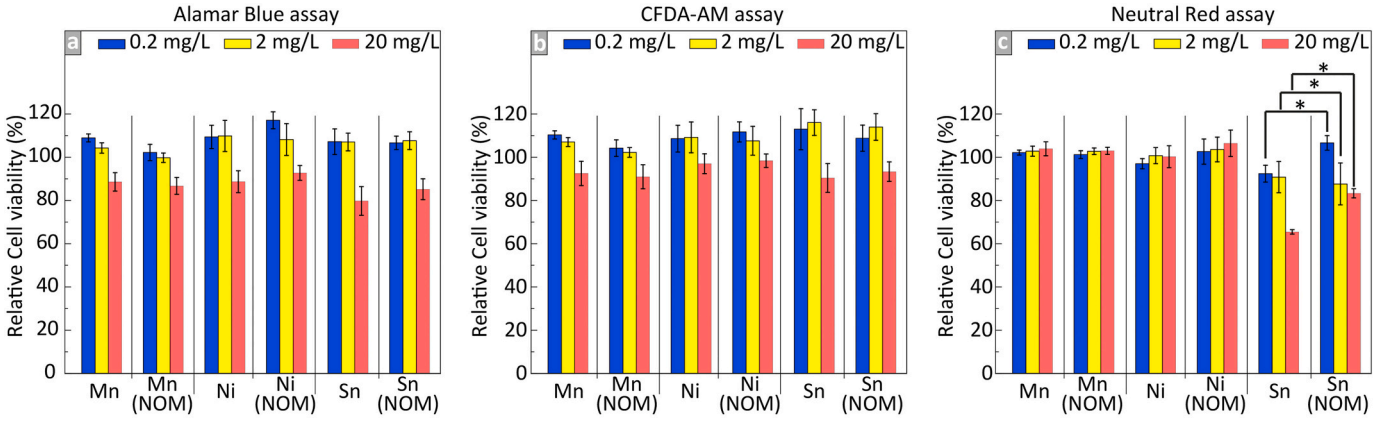

Fig. 8. Relative viability of RTL-W1 after 24 h exposure to increasing concentrations of Mn, Ni and Sn NPs in FW with and without NOM. Cytotoxicity of the respective NP was assessed by means of (a): Alamar Blue, (b): CFDA-AM, and (c): Neutral red fluorescent probes. Cells incubated with only medium (vehicle) served as negative control and used for normalization. The results represent the means of 3 repetitions, and the error bars represent standard errors of the means (SEM) of at least three independent experiments. Statistical significance between the groups are indicated as * $p < 0.05$, ** $p < 0.01$ (Student's t-test and one-way ANOVA). (For interpretation of the references to colour in this figure legend, the reader is referred to the web version of this article.)

consumption of reagent during the measurements (Kessler et al., 2021).

As illustrated in Fig. 8, a general reduction in cell viability was observed with increased NP concentration. All particles showed a similar decreasing trend regardless of the presence of NOM with increasing NP dose.

It has been proven that no toxicity mechanism can be considered generic for all NPs, although oxidative stress is frequently reported as one underlying mechanism. Generated results show that the trends in cytotoxicity for the investigated particles, Fig. 8, did not match the generation of ROS, Fig. 7. This indicates that the effects of the observed ROS generation may not be high enough to induce death, or the mechanisms by which the investigated NPs exert their toxic effects may not be due to oxidative stress. However, the higher generation rate of ROS observed for the Sn NPs compared to the Ni and Mn NPs is interesting. No previous evidence was identified to support the effects posed by the Sn NPs, although there seems to be a link between reduced cell viability, Fig. 8c and increased ROS generation, Fig. 7c. Further studies into establishing this relationship may be necessary to unambiguously conclude that oxidative stress may be the underlying mechanism by which lysosomal stability is affected by the Sn NPs. Studies on other NPs show that they exert their effects by interacting with cell-membrane proteins and infiltration of the cells, which lead to imbalances in the redox state of the cell, which further cause oxidative stress and cell damage (Tammina et al., 2017; Manke et al., 2013; Lin et al., 2008). The results of the Sn NPs seem to be in line with the current mechanism as we observed increased ROS and decreased cell viability. Similar results have been observed on exposure of TiO_2 and ZnO NPs on mouse macrophage Ana-1 cells, where remarkable increases in intracellular ROS were observed following cytotoxicity (Horie and Tabei, 2020).

Both the Alamar blue and CFDA-AM assays, Fig. 8a,b, used to detect changes in cellular metabolic activity and membrane integrity, showed similar trends for the three NPs with a dose-dependent reduction in cell viability. This was confirmed by optical microscopy, where signs of slight cell damage were observed at the highest dose (20 mg/L). The trends suggest a difference in cell viability upon the addition of NOM. However, since no statistically significant differences were observed between the NPs with and without adsorbed NOM, its role on cellular metabolic activity and membrane integrity seems small though needs further investigations.

Results of the Neutral Red assay, Fig. 8c, used to measure lysosomal membrane permeability and activity (Kamiloglu et al., 2020) in RTGill-W1 cells exposed to the 6 treatments, showed that cells were affected by the exposure to the Sn NPs, but no distinct differences were observed in contact with the Mn and Ni NPs, neither with nor without NOM. The gradual dose-dependent reduction in viability with increased dose indicated damage to lysosomal membranes. The lysosomes seem to be protected in the presence of NOM, though the protective effects observed as reduced cell viability was not as profound observed for the Sn NPs with and without NOM. The difference observed between the Sn NPs with and without NOM was statistically significant for the highest dose (20 mg/L, $p < 0.05$) and between the Sn NPs and the medium only ($p < 0.01$). This may also be linked to its dissolution profile, Fig. 6. The proposed link is based on the hypothesis that the reduction in viability (increased toxicity) in the presence of Sn NPs is mostly connected to the NPs themselves, which are expected to be translocated and stored in the lysosomes (Stern et al., 2012; Lammel et al., 2013), thereby disrupting their functions and cell processes. The metal ions which are readily available, as a result of increased dissolution with NOM, results in fewer Sn NPs, thereby, reducing the number of particles reaching the lysosomes and reducing the toxic impact on the cells. Only the Sn NP showed a positive correlation with an enhanced dissolution induced by the adsorption of NOM (shift in the asymmetric COO^- band). No distinct trends were observed for the Mn and Ni NPs, and no statistically significant results were observed with respect to the control. The effects observed could also be due to the interaction between NOM and dissoloved metal ions and this could be further investigated in future studies. From their patterns observed in Fig. 6, it was evident that the presence of NOM influenced the dissolution of the Sn NPs, which may explain the clear difference in cell viability observed in the presence of Sn NPs. No evidence of any NP interference with the assays was observed in the control measurements why this effect was excluded.

Mn NPs has been shown to induce acute toxicity *via* inhalation in both human and animal studies (Pradhan et al., 2014; Zaitseva et al., 2015). No evidence has though been brought forward to support the toxicity of Mn NPs in fish. Some studies suggest that macro-sized metal Mn may induce toxicity in the gills and liver of fish and in other aquatic species (Summer et al., 2019). The mechanism by which Mn NPs induces cellular toxicity has though not been established. Studies show Ni-induced cellular toxicity *via* apoptosis at doses between 25 and 100 μg/mL and potency to induce oxidative stress in human liver (HepG2) and lung epithelial (NCI-H460) cell lines (Wu and Kong, 2020). However, these doses are slightly higher than investigated in this study. This study shows that the Ni NPs, at given concentrations, result in cell death after 24 h but may also affect other sublethal endpoints. Repeated or long-term exposures were not conducted in this study and may hence be required to give an overall picture of the ecotoxic effects posed by the Ni NPs in a similar way as reported for zebrafish for which NP internalization was an important factor in toxicity and defects generated by the

NPs (Ispas et al., 2009). Reported studies on human A549 and HCT116 carcinoma cell lines have investigated the cytotoxic potency of SnO_2 NPs linked to the generation of ROS (Tammina et al., 2017). It was concluded that cytotoxicity was linked to the particle size as well as dosage and that ROS generation was responsible for the observed cytotoxic effects. Similar results have been reported for Mg NPs and Fe_2O_3 nanocomposites up to a dose of 100 mg/L (Watanabe et al., 2013) on A549 cells and for CeO_2 NPs on different cell lines at a minimum of 2 mg/L. (De Marzi et al., 2013) This study demonstrated the potential of Mn, Ni, and Sn NPs to generate ROS in piscine cells both in the presence and absence of NOM.

4. Summary

The effect of natural organic matter (NOM) on the environmental transformation and dissolution of diffusely dispersed engineered metal and metal oxide NPs of different surface and solubility properties was investigated in synthetic freshwater (FW). The prevailing trend was that NOM adsorbed to most NP surfaces regardless of zeta potential, creating a negatively charged colloid of smaller size compared with conditions in FW alone. The Sb and Sb_2O_3 NPs represented outliers, with minor adsorption of NOM, which was possibly connected to very low IEPs of the NPs and hence weaker NOM-NP interactions. The influence of NOM on particle dissolution correlated with the strength of interaction between the carboxylate group of NOM and the NP surface. Stronger interactions resulted in enhanced dissolution and *vice versa*. The results indicate that the use of polarizing power of metal ions can be a way forward to predict the effects of NOM on the dissolution pattern for metallic NPs and possibly an approach for grouping of metallic NPs even though differences in NP composition are not taken into account.

In vitro studies were performed using the piscine cell line RTGill-W1 to assess if weathering (transformation/dissolution) and adsorption of NOM to the NPs would influence the ecotoxic potency in terms of cytotoxicity, effects on membrane permeability, mitochondrial activity and lysosomal activity as well as their potential to generate ROS. All NPs generated intracellular ROS in a time and dose dependent manner. The extent of intracellular ROS generation in FW was similar for both Mn and Ni NPs (100 RFU), whereas a higher ROS level (150 RFU) were established for Sn NPs. Interactions and infiltration of the NPs with the cells lead to redox imbalances, which can further cause oxidative stress and cell damage. This may be the underlying mechanism for the investigated NPs (Sn, Mn and Ni). The results of the Sn NPs seem to be in line with this mechanism as increased ROS and decreased cell viability were observed. The presence of NOM generally reduced the intracellular ROS generation by 20–40% for the investigated NPs. In addition, the Sn NPs exhibited cytotoxic effects through action on the lysosomes. The presence of NOM actively reduced cytotoxicity, which can be attributed to the stronger interaction with the Sn NPs and hence increased dissolution. No such changes were observed for the Mn and Ni NPs.

In all, the results presented herein can be used to understand environmental fate effects of short-term transformation/dissolution processes for various metal and metal oxide NPs at environmentally relevant settings. Generated data is relevant for environmental risk assessments, useful to provide regulatory constraints or for predictive modelling of the fate of diffusely dispersed NPs, for example, to extrapolate measurements performed in FW to conditions of FW with NOM.

CRediT authorship contribution statement

Alexander Khort: Investigation, Data curation, Formal analysis, Visualization, Writing – original draft. **Marianne Brookman-Amissah:** Investigation, Formal analysis, Visualization, Writing – original draft. **Jonas Hedberg:** Methodology, Investigation, Formal analysis, Visualization, Supervision, Writing – original draft. **Tingru Chang:** Investigation, Writing – original draft. **Nanxuan Mei:** Investigation. **Annie Lundberg:** Investigation. **Joachim Sturve:** Methodology, Project administration, Supervision, Writing – review & editing. **Eva Blomberg:** Project administration, Methodology, Supervision, Writing – review & editing. **Inger Odnevall:** Methodology, Conceptualization, Funding acquisition, Project administration, Supervision, Writing – review & editing.

Declaration of Competing Interest

The authors declare that they have no known competing financial interests or personal relationships that could have appeared to influence the work reported in this paper.

Acknowledgements

This work forms part of the Mistra Environmental Nanosafety program, Sweden. Financial support from Mistra, the Swedish foundation for strategic environmental research, is highly acknowledged. Dr. Julian Gallego-Urrea and Dr. Samuel Mwaniki Gaita, Gothenburg University, are gratefully acknowledged for the ICP-MS analysis of Y and Ce. The JRC Repository (EU Commission) is greatly acknowledged for the supply of the CeO_2 and ZnO NPs.

We are also grateful to the Swedish Institute Visby Programme (grant 25897/2018) for financial support for Dr. Khort.

References

Arvidsson, R., Molander, S., Sandén, B.A., Hassellöv, M., 2011. Challenges in exposure modeling of nanoparticles in aquatic environments. Hum. Ecol. Risk. Assess. 17, 245–262.

Arvidsson, R., Hansen, S.F., Baun, A., 2020. Influence of natural organic matter on the aquatic ecotoxicity of engineered nanoparticles: recommendations for environmental risk assessment. NanoImpact 100263.

Borm, P., Klaessig, F.C., Landry, T.D., Moudgil, B., Pauluhn, J., Thomas, K., Trottier, R., Wood, S., 2006. Research strategies for safety evaluation of nanomaterials, part V: role of dissolution in biological fate and effects of nanoscale particles. Toxicol. Sci. 90, 23–32.

Brunauer, S., Emmett, P.H., Teller, E., 1938. Adsorption of gases in multimolecular layers. J. Am. Chem. Soc. 60, 309–319.

Bundschuh, M., Filser, J., Luderwald, S., McKee, M.S., Metreveli, G., Schaumann, G.E., Schulz, R., Wagner, S., 2018. Nanoparticles in the environment: where do we come from, where do we go to? Environ. Sci. Eur. 30, 6.

Cappellini, F., Hedberg, Y., Mc Carrick, S., Hedberg, Y., Derr, R., Hendriks, G., Odnevall Wallinder, I., Karlsson, H.L., 2018. Mechanistic insight into reactivity and (geno) toxicity of well-characterized nanoparticles of cobalt metal and oxides. Nanotoxicology. https://doi.org/10.1080/17435390.2018.1470694.

Chin, H.S., Cheong, K.Y., Razak, K.A., 2010. Review on oxides of antimony nanoparticles: synthesis, properties, and applications. J. Mater. Sci. 45, 5993–6008.

Clausen, L.P.W., Hansen, S.F., 2018. The ten decrees of nanomaterials regulations. Nat. Nanotechnol. 13, 766.

Dale, A.L., Lowry, G.V., Casman, E.A., 2015. Much ado about α: reframing the debate over appropriate fate descriptors in nanoparticle environmental risk modeling. Environ. Sci. Nano. 2, 27–32.

Dale, A.L., Lowry, G.V., Casman, E.A., 2017. Accurate and fast numerical algorithms for tracking particle size distributions during nanoparticle aggregation and dissolution. Environ. Sci. Nano. 4, 89–104.

Dayeh, V.R., Bols, N.C., Tanneberger, K., Schirmer, K., Lee, L.E., 2013. The use of fish-derived cell lines for investigation of environmental contaminants: an update following OECD's fish toxicity testing framework No. 171. Curr. Protoc. Toxicol. Chapter 1, Unit1 5.

De Marzi, L., Monaco, A., De Lapuente, J., Ramos, D., Borras, M., Di Gioacchino, M., Santucci, S., Poma, A., 2013. Cytotoxicity and genotoxicity of ceria nanoparticles on different cell lines in vitro. Int. J. Mol. Sci. 14, 3065–3077.

Furberg, A., Arvidsson, R., Molander, S., 2019. Dissipation of tungsten and environmental release of nanoparticles from tire studs: a Swedish case study. J. Clean. Prod. 207, 920–928.

Garner, K.L., Keller, A.A., 2014. Emerging patterns for engineered nanomaterials in the environment: a review of fate and toxicity studies. J. Nanopart. Res. 16, 2503.

Garner, K.L., Suh, S., Keller, A.A., 2017. Assessing the risk of engineered nanomaterials in the environment: development and application of the nanoFate model. Environ. Sci. Technol. 51, 5541–5551.

Gondikas, A., von der Kammer, F., Kaegi, R., Borovinskaya, O., Neubauer, E., Navratilova, J., Praetorius, A., Cornelis, G., Hofmann, T., 2018. Where is the nano? Analytical approaches for the detection and quantification of TiO_2 engineered nanoparticles in surface waters. Environ. Sci. Nano. 5, 313–326.

Gottschalk, F., Sun, T., Nowack, B., 2013. Environmental concentrations of engineered nanomaterials: review of modeling and analytical studies. Environ. Pollut. 181, 287–300.

Gulley-Stahl, H., Hogan, P.A., Schmidt, W.L., Wall, S.J., Buhrlage, A., Bullen, H.A., 2010. Surface complexation of catechol to metal oxides: an ATR-FTIR, adsorption, and dissolution study. Environ. Sci. Technol. 44, 4116–4121.
Hay, M.B., Myneni, S.C.B., 2007. Structural environments of carboxyl groups in natural organic molecules from terrestrial systems. Part 1: infrared spectroscopy. Geochim. Cosmochim. Acta 71, 3518–3532.
Hedberg, Y.S., Pradhan, S., Cappellini, F., Karlsson, M.-E., Blomberg, E., Karlsson, H., Odnevall Wallinder, I., Hedberg, J.F., 2016. Electrochemical surface oxide characteristics of metal nanoparticles (Mn, Cu and Al) and the relation to toxicity. Electrochim. Acta 212, 360–371.
Hedberg, Y.S., Hedberg, J.F., Isaksson, S., Mei, N., Blomberg, E., Wold, S., Odnevall Wallinder, I., 2017a. Odnevall Wallinder, nanoparticles of WC-Co, WC, Co and Cu of relevance for traffic wear particles - particle stability and reactivity in synthetic surface water and influence of humic matter. Environ. Pollut. 224, 275–288.
Hedberg, J., Ekvall, M., Hansson, L.-A., Cedervall, T., Odnevall Wallinder, I., 2017b. Tungsten carbide nanoparticles in simulated surface water with natural organic matter: dissolution, agglomeration, sedimentation and interaction with Daphnia magna. Environ. Sci. Nano. 4, 886.
Hedberg, J., Blomberg, E., Odnevall Wallinder, I., 2019. In the search for Nanospecific effects of dissolution of metallic nanoparticles at freshwater-like conditions: a critical review. Environ. Sci. Technol. 53, 4030–4044.
Horie, M., Tabei, Y., 2020. Role of oxidative stress in nanoparticles toxicity. Free Radic. Res. 1–12. https://doi.org/10.1080/10715762.2020.1859108.
Hotze, E.M., Phenrat, T., Lowry, G.V., 2010. Nanoparticle aggregation: challenges to understanding transport and reactivity in the environment. J. Environ. Qual. 39, 1909–1924.
Hug, S.J., Sulzberger, B., 1994. In situ Fourier transform infrared spectroscopic evidence for the formation of several different surface complexes of oxalate on TiO_2 in the aqueous phase. Langmuir 10, 3587–3597.
Ispas, C., Andreescu, D., Patel, A., Goia, D.V., Andreescu, S., Wallace, K.N., 2009. Toxicity and developmental defects of different sizes and shape nickel nanoparticles in zebrafish. Environ. Sci. Technol. 43, 6349–6356.
Johnson, S.B., Yoon, T.H., Brown, G.E., 2005. Adsorption of organic matter at mineral/water interfaces: 5. Effects of adsorbed natural organic matter analogues on mineral dissolution. Langmuir 21, 2811–2821.
Johnston-Peck, A.C., Wang, J., Tracy, J.B., 2009. Synthesis and structural and magnetic characterization of Ni (Core)/NiO (Shell) nanoparticles. ACS Nano 3, 1077–1084.
Kamiloglu, S., Sari, G., Ozdal, T., Capanoglu, E., 2020. Guidelines for cell viability assays. Food Front. 1, 332–349.
Kent, R.D., Vikesland, P.J., 2016. Dissolution and persistence of copper-based nanomaterials in undersaturated solutions with respect to cupric solid phases. Environ. Sci. Technol. 50, 6772–6781.
Kessler, A., Hedberg, J., McCarrick, S., Karlsson, H.L., Blomberg, E., Odnevall, I., 2021. Adsorption of horseradish peroxidase on metallic nanoparticles: effects on reactive oxygen species detection using 2′,7’-Dichlorofluorescin diacetate. Chem. Res. Toxicol. 34, 1481–1495.
Khort, A., Podbolotov, K., Serrano-García, R., Gun’ko, Y., 2018. One-step solution combustion synthesis of cobalt nanopowder in air atmosphere: the fuel effect. Inorg. Chem. 57, 1464–1473.
Khort, A., Hedberg, J., Mei, N., Romanovski, V., Blomberg, E., Odnevall, I., 2021. Corrosion and transformation of solution combustion synthesized Co, Ni and CoNi nanoparticles in synthetic freshwater with and without natural organic matter. Sci. Rep. 11, 7860.
Kosmulski, M., 2009. Compilation of PZC and IEP of sparingly soluble metal oxides and hydroxides from literature. Adv. Colloid Interf. Sci. 152, 14–25.
Lammel, T., Boisseaux, P., Fernandez-Cruz, M.L., Navas, J.M., 2013. Internalization and cytotoxicity of graphene oxide and carboxyl graphene nanoplatelets in the human hepatocellular carcinoma cell line Hep G2. Part Fibre Toxicol 10, 27.
Latvala, S., Hedberg, J., Di Bucchianico, S., Möller, L., Odnevall Wallinder, I., Elihn, K., Karlsson, H.L., 2016. Nickel release, ROS generation and toxicity of Ni and NiO Micro-and nanoparticles. PLoS One 11, e0159684.
Lefèvre, G., 2004. In situ Fourier-transform infrared spectroscopy studies of inorganic ions adsorption on metal oxides and hydroxides. Adv. Colloid Interf. Sci. 107, 109–123.
Lin, W., Stayton, I., Huang, Y.-W., Zhou, X.-D., Ma, Y., 2008. Cytotoxicity and cell membrane depolarization induced by aluminum oxide nanoparticles in human lung epithelial cells A549. Toxicol. Environ. Chem. 90, 983–996.
Lowry, G.V., 2018. Inching closer to realistic exposure models. Nat. Nanotechnol. 13, 983–985.
Lowry, G.V., Gregory, K.B., Apte, S.C., Lead, J.R., 2012. Transformations of nanomaterials in the environment. Environ. Sci. Technol. 46, 6893–6899.
Lynch, I., Dawson, K., Lead, J., Valsami-Jones, E., 2014a. Macromolecular Coronas and their Importance in Nanotoxicology and Nanoecotoxicology, Frontiers of Nanoscience. Elsevier, Amsterdam.
Lynch, I., Dawson, K.A., Lead, J.R., Valsami-Jones, E., 2014b. In Nanoscience and the Environment, eds. J. R. Lead and E. Valsami-Jones, 7. Elsevier, pp. 127–156 ch. 4.
Manke, A., Wang, L., Rojanasakul, Y., 2013. Mechanisms of nanoparticle-induced oxidative stress and toxicity. Biomed. Res. Int. 2013, 942916.
McCarrick, S., Cappellini, F., Kessler, A., Moelijker, N., Derr, R., Hedberg, J., Wold, S., Blomberg, E., Odnevall Wallinder, I., Hendriks, G., 2020. ToxTracker reporter cell lines as a tool for mechanism-based (geno) toxicity screening of nanoparticles–metals, oxides and quantum dots. Nanomaterials 10, 110.
Monikh, F.A., Praetorius, A., Schmid, A., Kozin, P., Meisterjahn, B., Makarova, E., Hofmann, T., von der Kammer, F., 2018. Scientific rationale for the development of an OECD test guideline on engineered nanomaterial stability. NanoImpact 11, 42–50.
Mudunkotuwa, I.A., Grassian, V.H., 2015. Biological and environmental media control oxide nanoparticle surface composition: the roles of biological components (proteins and amino acids), inorganic oxyanions and humic acid. Environ. Sci. Nano. 2, 429–439.
Mudunkotuwa, I.A., Al Minshid, A., Grassian, V.H., 2014. ATR-FTIR spectroscopy as a tool to probe surface adsorption on nanoparticles at the liquid–solid interface in environmentally and biologically relevant media. Analyst 139, 870–881.
Nielsen, M.B., Baun, A., Mackevica, A., Thit, A., Odnevall Wallinder, I., Gallego, J.A., Westergaard Clausen, L.P., Rissler, J., Skjolding, L., Castro Nilsson, A., Cedervall, T., Foss Hansen, S., 2021. Nanomaterials in the European chemicals legislation – methodological challenges for registration and environmental safety assessment. Environ. Sci. Nano. https://doi.org/10.1039/d0en01123a.
OECD, 2002. Guidance Document on Transformation/Dissolution of Metals and Metal Compounds in Aqueous Media.
OECD, 2017. Test No. 318: Dispersion Stability of Nanomaterials in Simulated Environmental Media.
Oriekhova, O., Stoll, S., 2016. Effects of pH and fulvic acids concentration on the stability of fulvic acids–cerium (IV) oxide nanoparticle complexes. Chemosphere 144, 131–137.
Petosa, A.R., Jaisi, D.P., Quevedo, I.R., Elimelech, M., Tufenkji, N., 2010. Aggregation and deposition of engineered nanomaterials in aquatic environments: role of physicochemical interactions. Environ. Sci. Technol. 44, 6532–6549.
Pradhan, S., Patra, P., Mitra, S., Dey, K.K., Jain, S., Sarkar, S., Roy, S., Palit, P., Goswami, A., 2014. Manganese nanoparticles: impact on non-nodulated plant as a potent enhancer in nitrogen metabolism and toxicity study both in vivo and in vitro. J. Agric. Food Chem. 62, 8777–8785.
Pradhan, S., Hedberg, J., Blomberg, E., Wold, S., Odnevall Wallinder, I., 2016. Odnevall Wallinder, effect of sonication on particle dispersion, administered dose and metal release of non-functionalized, non-inert metal nanoparticles. J. Nanopart. Res. 18, 285.
Pradhan, S., Hedberg, J., Rosenqvist, J., Jonsson, C.M., Wold, S., Blomberg, E., Odnevall Wallinder, I., 2018. Odnevall Wallinder, influence of humic acid and dihydroxy benzoic acid on the agglomeration, adsorption, sedimentation and dissolution of copper, manganese, aluminum and silica nanoparticles – a tentative exposure scenario. PLoS One 13, e0192553.
Ritchie, J.D., Perdue, E.M., 2003. Proton-binding study of standard and reference fulvic acids, humic acids, and natural organic matter. Geochim. Cosmochim. Acta 67, 85–96.
Schirmer, K., Chan, A.G.J., Greenberg, B.M., Dixon, D.G., Bols, N.C., 1997. Methodology for demonstrating and measuring the photocytotoxicity of fluoranthene to fish cells in culture. Toxicol. in Vitro 11, 107–119.
Schneckenburger, T., Lattao, C., Pignatello, J.J., Schaumann, G.E., Thiele-Bruhn, S., Cao, X., Mao, J., 2012. Preparation and characterization of humic acid cross-linked with organic bridging groups. Org. Geochem. 47, 132–138.
Shannon, R.D., 1976. Revised effective ionic radii and systematic studies of interatomie distances in halides and chaleogenides. Acta Crystallogr. A 32, 751–767.
Stern, S.T., Adiseshaiah, P.P., Crist, R.M., 2012. Autophagy and lysosomal dysfunction as emerging mechanisms of nanomaterial toxicity. Part Fibre Toxicol 9, 20.
Stumm, W., 1995. In Aquatic Chemistry: Interfacial and Interspecies Processes. American Chemical Society, USA, pp. 1–32. https://doi.org/10.1021/ba-1995-0244.ch001 ch. 1.
Summer, K., Reichelt-Brushett, A., Howe, P., 2019. Toxicity of manganese to various life stages of selected marine cnidarian species. Ecotoxicol. Environ. Saf. 167, 83–94.
Svendsen, C., Walker, L.A., Matzke, M., Lahive, E., Harrison, S., Crossley, A., Park, B., Lofts, S., Lynch, I., Vázquez-Campos, S., 2020. Key principles and operational practices for improved nanotechnology environmental exposure assessment. Nat. Nanotechnol. 1–12.
Tammina, S.K., Mandal, B.K., Ranjan, S., Dasgupta, N., 2017. Cytotoxicity study of *Piper nigrum* seed mediated synthesized SnO2 nanoparticles towards colorectal (HCT116) and lung cancer (A549) cell lines. J. Photochem. Photobiol. B 166, 158–168.
Traina, C.A., Schwartz, J., 2007. Surface modification of Y_2O_3 nanoparticles. Langmuir 23, 9158–9161.
Tsao, T.M., Chen, Y.M., Wang, M.K., 2011. Origin, separation and identification of environmental nanoparticles: a review. J. Environ. Monit. 13, 1156–1163.
Turan, N.B., Erkan, H.S., Engin, G.O., Bilgili, M.S., 2019. Nanoparticles in the aquatic environment: usage, properties, transformation and toxicity – a review. Process. Saf. Environ. Prot. 130, 238–249.
Vance, M.E., Kuiken, T., Vejerano, E.P., McGinnis, S.P., Hochella Jr., M.F., Rejeski, D., Hull, M.S., 2015. Nanotechnology in the real world: redeveloping the nanomaterial consumer products inventory. Beilstein J. Nanotechnol. 6, 1769–1780.
Vencalek, B.E., Laughton, S.N., Spielman-Sun, E., Rodrigues, S.M., Unrine, J.M., Lowry, G.V., Gregory, K.B., 2016. In situ measurement of CuO and $cu(OH)_2$ nanoparticle dissolution rates in quiescent freshwater Mesocosms. Environ. Sci. Technol. Lett. 3, 375–380.
Wang, Z., Zhang, L., Zhao, J., Xing, B., 2016. Environmental processes and toxicity of metallic nanoparticles in aquatic systems as affected by natural organic matter. Environ. Sci. Nano. 3, 240–255.
Watanabe, M., Yoneda, M., Morohashi, A., Hori, Y., Okamoto, D., Sato, A., Kurioka, D., Nittami, T., Hirokawa, Y., Shiraishi, T., Kawai, K., Kasai, H., Totsuka, Y., 2013. Effects of Fe3O4 magnetic nanoparticles on A549 cells. Int. J. Mol. Sci. 14, 15546–15560.
Wu, Y., Kong, L., 2020. Advance on toxicity of metal nickel nanoparticles. Environ. Geochem. Health 42, 2277–2286.
Xu, L., Xu, M., Wang, R., Yin, Y., Lynch, I., Liu, S., 2020. The crucial role of environmental coronas in determining the biological effects of engineered nanomaterials. Small 2003691.

Yoon, T.H., Johnson, S.B., Brown, G.E., 2005. Adsorption of organic matter at mineral/water interfaces. IV. Adsorption of humic substances at boehmite/water interfaces and impact on boehmite dissolution. Langmuir 21, 5002–5012.
Zaitseva, N.V., Zemlyanova, M.A., Zvezdin, V.N., Akafieva, T.I., Saenko, E.V., 2015. Acute inhalation toxicity of manganese oxide nanoparticles. Nanotechnol. Russia 10, 468–474.
Zhang, W.M., Hu, J.S., Guo, Y.G., Zheng, S.F., Zhong, L.S., Song, W.G., Wan, L.J., 2008. Tin-nanoparticles encapsulated in elastic hollow carbon spheres for high-performance anode material in lithium-ion batteries. Adv. Mater. 20, 1160–1165.
Zhang, F., Wang, Z., Wang, S., Fang, H., Chen, M., Xu, D., Tang, L., Wang, D., 2016. Physicochemical properties and ecotoxicological effects of yttrium oxide nanoparticles in aquatic media: role of low molecular weight natural organic acids. Environ. Pollut. 212, 113–120.